RESEARCH ON MODELING THE TEMPERATURE FIELD OF A NEW AEROSPACE SERVO ELECTRO-HYDROSTATIC MODULE BASED ON THERMO-MAGNETIC BIDIRECTIONAL COUPLING ANALYSIS

Xintong HU[1], Yongling FU[1], Dingchong LYU[1], Mingwei SUN[1], Shoujun ZHAO[2], Jian FU[1], Jiangao ZHAO[1]

[1]School of Mechanical Engineering and Automation, Beihang University, Beijing 100191, CHINA
[2] Beijing Institute of Precision Mechatronics and Controls, Laboratory of Aerospace Actuation and Transmission, Beijing, 100076, CHINA

Abstract

The highly compact Electro-Hydrostatic Module (EHM) is a key technology for future Electro-Hydrostatic Actuation (EHA) in the aerospace industry. Analyzing and improving the heat dissipation capability is crucial for EHM. In order to accurately analyze the temperature distribution of EHM under various operating conditions, a new evaluation method for friction losses of EHM under mixed friction conditions is proposed. A multi-physics coupling method, including flow field, electromagnetic field, and temperature field, is introduced for temperature rise calculation. The electromagnetic losses obtained from electromagnetic analysis are directly mapped to the temperature field and incorporated into the boundary conditions of the flow field through multiple iterative couplings. This paper compares the thermal analysis results of two different temperature rise calculation methods, analyzes the temperature distribution of EHM under different operating conditions, and discusses the simulation results in comparison with experimental measurements. The multi-physics coupling simulation method demonstrates an accuracy improvement of 17.58% compared to the traditional approach, validating the superiority of the proposed coupling analysis method in enhancing the accuracy of motor temperature rise calculation. From the perspectives of reliability and efficiency, this research provides theoretical reference points for thermal management of novel EHM.

Keywords: EHA, servo electro-hydrostatic module, thermal management, Magne-thermal bidirectional coupling, finite element method, CFD

1. General Introduction

In recent years, electrostatic hydraulic actuators (EHA) have gained increasing prominence across diverse fields, owing to their commendable attributes such as high efficiency, reliability, and facile maintenance[1]-[6]. At the heart of the EHA system, the Electro-Hydrostatic Module (EHM) plays a pivotal role in defining the upper threshold of the EHA's output performance. The motor within this component transforms electrical energy into rotational speed and torque, thereby enabling the pump to generate the desired flow and pressure. The configuration of the EHA and EHM is visually depicted in Figure 1.

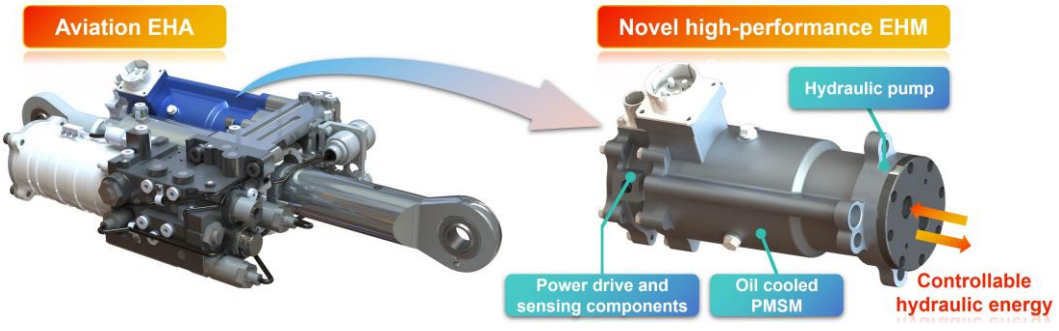

Figure 1 – Configurations of EHA and motor-pump assembly[1]

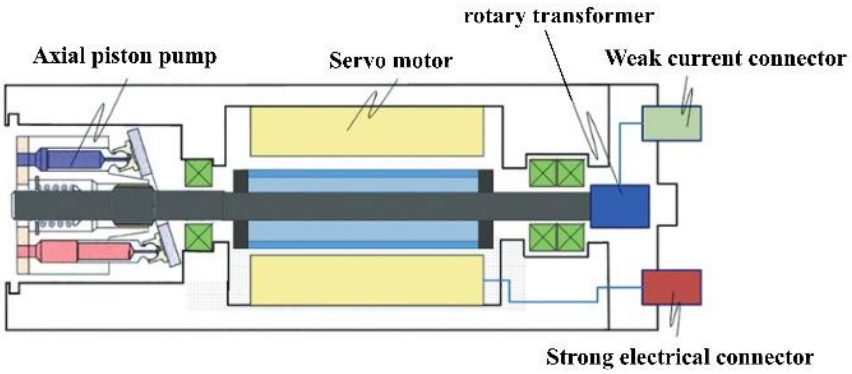

Figure 2 –Internal structure of the coaxial co-casing EHM [7]

The EHM represents a novel form of electro-hydraulic power unit, seamlessly combining the hydraulic pump, wet motor, and drive electronics to address the drawbacks associated with the traditional "three-stage" pump source, including large volume, high weight, elevated noise levels, significant leakage, low efficiency, and suboptimal dynamic characteristics (refer to Figure 2). In this innovative assembly, the integration of the motor and pump is achieved through two distinct modes. First, by eliminating the axial connection between the motor and pump, the hydraulic pump rotor is integrated onto the motor rotor, and the dynamic sealing between the motor and hydraulic pump is eliminated. Second, the assembly adopts a coaxial co-housing integration mode, where the hydraulic pump and the motor rotor share a coaxial housing (as illustrated in Figure 2). This design marks a significant departure from conventional configurations, offering a more compact, efficient, and noise-resistant solution. Owing to its absence of external leakage, reduced noise levels, and enhanced motor heat dissipation, the latter structure, employing the coaxial co-housing integration mode, has found widespread application in demanding sectors such as aerospace[1][2][8][9][11]. The object of this study is the coaxial integrated EHM applied to the aileron Electro-Hydrostatic Actuator (EHA) on civil aircraft, as shown in Figure 3. Due to the rapid variation of aerodynamic loads during mission processes[2], the EHM needs to face operating conditions characterized by 'high frequency, wide range, and constant changes.' Additionally, the EHM is small in size, with a compact arrangement of internal components.

Figure 3 – The application scenario and structural characteristics of the EHM

The thermal coupling between the pump and motor in the new integrated form of the EHM component, where a large flow field exists coaxially, causes heat generation through flow field interaction. It is unknown whether this temperature coupling has a significant impact on the thermal characteristics of the two components. Furthermore, due to the small size and compact structure of the new EHM, the heat generation and cooling of highly integrated hydraulic EHM have become a pressing issue to be addressed [12]. The thermal characteristics within the cavity have been proven to have a significant influence on its performance operating at high speeds, various losses[13] (refer to Table 1) become predominant factors influencing the performance of high-speed servo EHM[7]. These

losses manifest as heat generation at different sites within the EHM, leading to a deterioration in overall performance. Notably, the diminished bearing capacity of the oil film between friction pairs in the hydraulic pump results in lubrication failure and increased wear[14]. Additionally, the high-speed operation of the wet motor's stator and rotor introduces substantial stirring losses in the oil gap, elevating temperatures on the rotor surface[15]. This heightened temperature poses risks to the permanent magnet and undermines the long-term stability of rotor operation. Furthermore, the elevated motor temperature accelerates the aging of winding insulation materials, significantly diminishing insulation performance and consequently reducing the motor's service life[16]. Hence, the central objectives of this research revolve around the establishment of an evaluation method for energy consumption in transient wide-range unsteady states. The aim is to discern the heat generation and heat dissipation mechanisms inherent to each component of the EHM. By doing so, the research endeavors to optimize the thermal characteristics of the EHM, ultimately enhancing its overall performance. In addressing these crucial aspects, the study seeks to contribute valuable insights into the efficient management of energy consumption and thermal dynamics in the transient and wide-ranging operational states of the EHM.

Table 1 The factors that may affect the thermal characteristics of integrated EHM[13]

Friction heat	Electromagnetic heating	Other factors
1) Mechanical friction	1) Iron loss	1) Leakage loss of friction pair
2) Power loss of friction pair	2) Copper loss	2) Throttle loss of damping hole
3) Stirring loss (stirring effect of cylinder and piston/slider pair)	3) Stirring loss of motor rotor	
	4) Stray losses	

In the thermal field modeling research of EHM, the computational fluid dynamics (CFD) method can provide accurate flow field characteristics. By combining material properties, the convective heat transfer coefficient between fluid and solid can be calculated. Utilizing the electromagnetic field finite element method (FEM) calculation to obtain the electromagnetic heat generation as thermal input can yield more accurate temperature prediction results, which greatly helps in understanding the complex coupling of heat generation and heat transfer mechanisms inside EHM. Reference [17] conducted simulation studies on the flow and temperature distribution in the cavity of a three-phase asynchronous motor-axial piston electro-hydraulic pump (EHP) housing. Reference [18] and others established a temperature field model of EHM based on Newton's cooling law and used CFD simulation software to investigate the influence of different heat dissipation structural parameters on the heat dissipation performance of EHM. Reference [12] established mathematical models for the flow field, electromagnetic field, and temperature field of hydraulic EHM; numerical simulations were used to study the distribution and coupling factors of the flow field, electromagnetic field, and temperature field of hydraulic EHM, as well as to verify the performance of heat dissipation structures. However, previous studies on EHM did not consider the impact of changes in the mixed friction state of hydraulic pumps under variable operating conditions on the overall heat generation. Furthermore, since the thermal analysis of the motor reflects the interaction of electromagnetic fields, temperature fields, and fluid fields, it cannot be simply superimposed. The increase in temperature has a certain influence on material properties, loss distribution, and flow field conditions, and the electromagnetic loss determines the heat source of the temperature field [19]. Hu et al. [20] and Guo et al. [21] conducted bidirectional thermal-magnetic coupling studies on high-speed magnetic levitation motors and hub motors for electric vehicles, respectively, considering the influence of temperature rise on material heat generation characteristics. They verified that this method has a good effect on improving the accuracy of thermal simulation models. Additionally, since most EHA (electro-hydraulic actuator) EHM are designed for overload to meet short-term high power requirements while reducing weight, the electromagnetic losses during overload account for a significant portion of the total losses. Therefore, it is necessary to conduct modeling and research on electromagnetic bidirectional coupling for EHM.

This study focuses on an integrated servo EHM used in the aileron electro-hydraulic actuator (EHA) for commercial aircraft, and it investigates the losses and temperature rise characteristics of the EHM. The influence of temperature on the electromagnetic characteristics of the magnets is analyzed in detail using Maxwell's electromagnetic method, considering the iron losses, copper losses, and eddy

current losses of the magnets. The ANSYS-Workbench platform is utilized for data transfer and to consider the non-uniform distribution of losses in different components during the actual operation of the motor. Combined with previous research, the friction losses under variable operating conditions are calculated using experimentally obtained mixed friction coefficients of the spool valve, and the impact of the friction state of critical friction pairs under variable operating conditions on heat generation is taken into account. By improving the accuracy of motor losses and temperature rise calculations, the study reveals the heat generation trends and mechanisms of the EHM under variable operating conditions. The modifications made in this study are summarized in Figure 4.

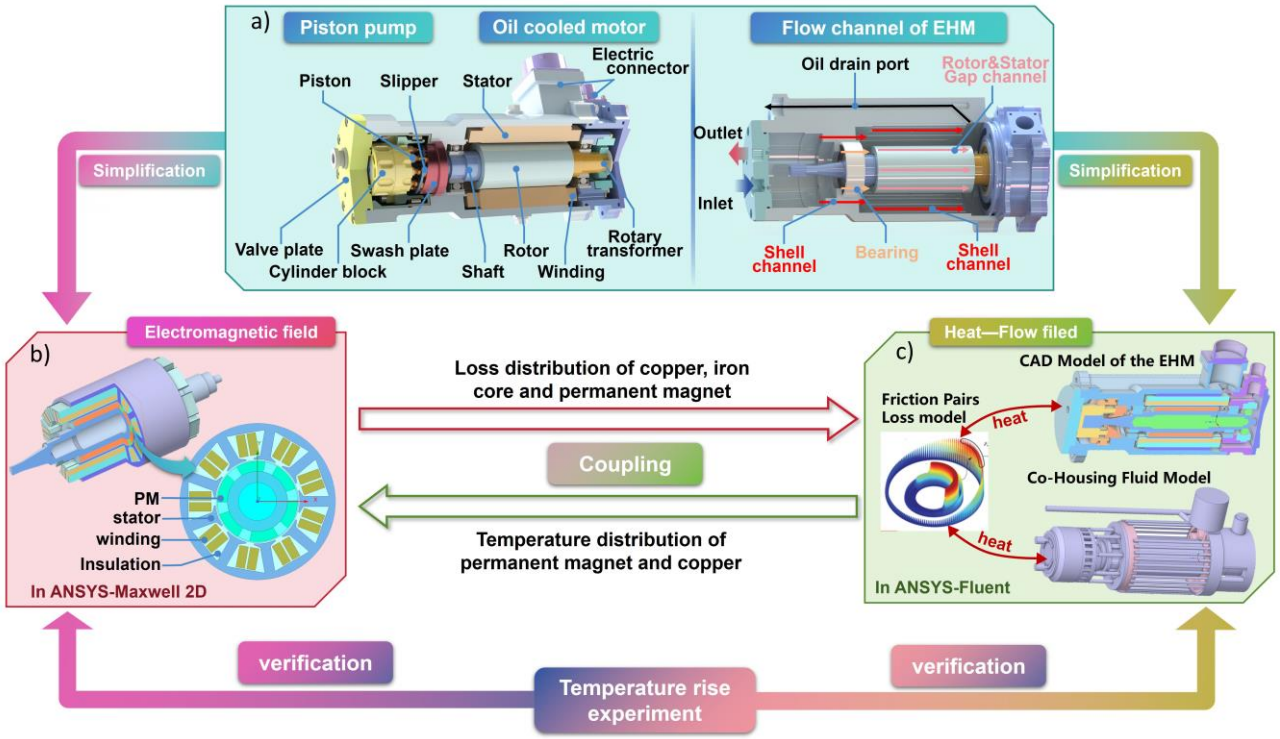

Figure 4 – The paper structure

2. Models and methods

2.1 Physical model and operation condition

The 3D structure of the EHM is shown in Figure 4. It mainly consists of the axial piston pump component, wet-type permanent magnet synchronous motor component, sensing and measurement components (thermocouples and rotary sensors), and power drive components. The motor rotor and the cylinder block piston shoe assembly of the pump are connected by a main shaft and supported by a pair of angular contact bearings to improve dynamic characteristics. The cylinder block is additionally supported by ball bearings. The EHM housing is designed in a corrugated manner to increase the heat dissipation area. Heat dissipation channels are created inside the EHM housing, in contact with the motor stator. The oil outlet is located at the end of the heat dissipation channels, establishing an internal leakage path for hydraulic oil to facilitate the removal of heat through the flow channels and the air gap between the motor stator and rotor, which helps dissipate heat from the leaking hydraulic oil of the piston pump. Samarium-cobalt (SmCo26H) magnet material is used, which can withstand operating temperatures of up to 350°C and reduces the risk of demagnetization under high-speed operation. The rotor adopts a sleeve structure to ensure that the permanent magnet is not damaged under high-speed operating conditions. The basic design parameters are shown in Table 2.

Table 2 Main design parameters of the EHM

Parameters	unit	Values
Rated power	kW	5.5
Rated speed	rpm	12500

Theoretical displacement of EHM	ml/r	1.845
Rated voltage	V	270DC
Winding layer		2
Slot number		9
Stator outer diameter	mm	74
Stator inter diameter	mm	40
Rotor outer diameter	mm	38
Rotor inter diameter	mm	18
Poles number		3
Core length	mm	80
Constant rotor clearance	mm	05
Thickness of PM	mm	4.8

To meet the requirements of rapid actuation, the EHM needs to have the ability to operate in a wide range of operating conditions. Its three main operating points are shown in Table 3:

Table 3 operating condition of EHM

Operating points	Unit	operating condition I Low speed high torque	operating condition II unloaded	operating condition III High speed low torque
Bus voltage	VDC	270	270	270
Bus current	A	15	6.4	21
Inlet and outlet pressure difference	MPa	34	1	10.78
Outlet flow	L/min	0.45	21.14	21.14
Rotational velocity	rpm	1400	12100	12500
Motor operating torque	Nm	11.6	0.98	3.72

2.2 Mathematic model

2.2.1 Temperature Field Mathematical Model

In the analysis of motor temperature rise, based on the law of heat exchange, when the variation of thermal conductivity with temperature is not considered, the mathematical model for calculating the three-dimensional temperature field can be expressed as follows:

$$\rho c \frac{\partial T}{\partial t} = \lambda \left(\frac{\partial^2 T}{\partial x^2} + \frac{\partial^2 T}{\partial y^2} + \frac{\partial^2 T}{\partial z^2} \right) + \rho q \tag{1}$$

$$\lambda \left(\frac{\partial T}{\partial x} n_x + \frac{\partial T}{\partial u} n_y + \frac{\partial T}{\partial z} n_z \right) = \alpha \left(T_w - T_f \right) \tag{2}$$

Where ρ is the density; c is the specific heat; T is the temperature; t is the time; λ is the thermal conductivity; q is the heat generation rate; n_x, n_y, and n_z are the normal vectors; α is the convective heat transfer coefficient; T_w is the temperature of the solid; T_f is the temperature of the fluid.

2.2.2 Basic Equations of Fluid Flow

In the fluid field, the continuity equation and the motion equation are used to calculate the velocity distribution of the fluid:

$$\frac{\partial \rho}{\partial t} + \frac{\partial (\rho \mu_j)}{\partial x_j} = 0 \tag{3}$$

$$\frac{\partial (\rho \mu)}{\partial \mathrm{t}} + \frac{\partial (\rho \mu_j \mu)}{\partial x_j} = \frac{\partial}{\partial x_j} \left(\mu \frac{\partial \mu}{\partial x_j} \right) + \rho f_x - \frac{\partial p}{\partial x} \tag{4}$$

$$\frac{\partial (\rho T)}{\partial t} + \frac{\partial (\rho \mu_j T)}{\partial x_j} = \frac{\partial}{\partial x_j} \left(\frac{\lambda}{c_v} . \frac{\partial T}{\partial x_j} \right) + \rho (q + T) / c_v \tag{5}$$

Where p is the fluid pressure, the subscript j represents spatial direction, and c_v is the constant volume specific heat capacity of an ideal gas.

2.2.3 The EHM loss Mode

The losses of EHM can mainly be divided into three parts: volumetric losses, mechanical losses, electromagnetic losses, and other losses. In the volumetric losses of EHM, leakage losses of the distribution sub-flow account for a significant portion objectively [22], so only the distribution sub-flow is considered in the volumetric losses. Mechanical losses include stirring losses of various rotor

components, viscous friction losses of various pump friction pairs, and mechanical friction losses of various pump friction pairs. Electromagnetic losses include copper losses, iron losses, permanent magnet eddy current losses, and stray losses, as summarized in Figure 5 (b). The uncontrollable stray losses are neglected in this study.

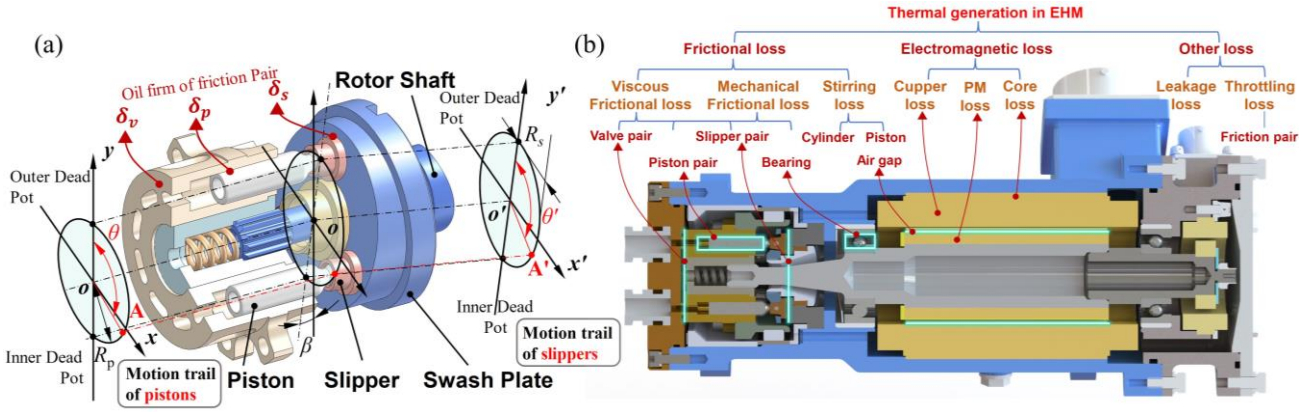

Figure 5 – (a) Main structural parameters of the EHM (b)Types of Losses in the EHM

1) Volumetric Losses

Leakage losses can be expressed as the product of the leakage flow rate and the pressure difference, that is:

$$p_{\mathrm{lv}} = Q_{lv} \times \Delta p \tag{6}$$

where Q_{lv} represents the leakage flow rate of the distribution sub-flow, obtained through simulation using an AMESim model[22] developed in previous studies, and Δp represents the pressure difference between the inside and outside of the distribution sub-flow.

2) Friction Loss

During the normal operation of the axial piston pump, the collision between the cylinder block and the valve plate leads to a complex boundary/mixed friction state at the interface. There are two commonly used calculation methods for the friction loss of the axial piston pump: one method considers the mechanical loss as the sum of the viscous loss generated by the friction force between the friction pairs in the oil film and the Coulomb friction loss under the fluid hydrostatic support:

$$p_1 = p_{\mathrm{c}} + p_{\mathrm{v}} \tag{7}$$

Since the Coulomb friction coefficient under fluid hydrostatic support is a constant value, this method cannot reflect the changes in the mixed friction state of the friction pairs under variable operating conditions. The second calculation method is based on the mixed friction coefficient μ_a as a variable characterizing the mixed friction state between the friction pairs. Its value lies between the Coulomb friction coefficient μ_c and the viscous friction coefficient μ_v and is an artificially specified value synthesized from the two under different proportions ξ :

$$\mu_a = \xi\mu_c + (1-\xi)\mu_v \tag{8}$$

The friction loss can be represented as the product of the mixed friction coefficient and the positive pressure:

$$p_2 = \mu_a \times N \tag{9}$$

In this way, by obtaining the mixed friction coefficient of the same friction pair under different operating conditions through experiments or model simulations, it is possible to characterize the friction loss under different mixed friction states, thereby providing a detailed description of the friction loss in the axial piston pump. However, this method requires a certain experimental basis. In previous studies [22], friction simulation experiments were conducted on the valve plate of the EHM studied in this paper. The mixed friction coefficients of this friction pair at different speeds were obtained. Considering that this friction pair has the highest heat generation among the friction pairs in the axial piston pump, the mechanical loss of this friction pair was calculated using The second calculation method, while The first calculation method was used to calculate the mechanical losses of the other

friction pairs.

a) Viscous friction loss at the piston pair:

$$p_{vp} = \frac{\mu q_t^2 l_H \omega^2}{2Z\pi R_p^3 \delta_p} \tag{10}$$

where: q_t is the theoretical displacement of the pump, l_H is the contact length between the piston and the cylinder block when the swash plate inclination angle is 0, δ_p is the piston pair oil film thickness.

b) Viscous friction loss at the slipper pair:

$$p_{vs} = \frac{\pi(R_{s2}^2 - R_{s1}^2) R_p^2 Z \mu \omega^2}{\delta_s \cos\beta} \tag{11}$$

where: δ_s is the clearance thickness of the slipper pair oil film, R_{s1} and R_{s2} are the diameters of the inner and outer sealing strips of the slipper, β is the swash plate inclination angle, Z is the number of pistons, R_p is the piston pitch circle radius.

c) Mechanical friction loss at the piston pair:

$$p_{cp} = f_{cp} m_{ps} \omega^3 R_p^2 \tan\beta \sum_{i=0}^{Z-1} \left|\sin\left(\varphi + \frac{2\pi}{Z} i\right)\right| \tag{12}$$

where: f_{cp} is the friction coefficient between the piston and the cylinder block, m_{ps} is the piston mass, φ is the angle rotated by the plunger from the starting position.

d) Mechanical friction loss at the slipper pair:

$$p_{cf} = \frac{Z\pi(R_{s2}^2 - R_{s1}^2) R_{pd} f_{cs}}{4\ln(R_{s2}/R_{s1})} \boldsymbol{\omega} \Delta p \tag{13}$$

where: f_{cs} is the friction coefficient between the two materials of the slipper pair.

e) Mechanical friction loss at the ball joint of the slipper pair:

$$p_{ch} = \frac{Z\omega\pi d_d^2 R_p f_{ch}}{8\cos\beta} \Delta p \tag{14}$$

where: f_{ch} is the friction coefficient between the piston and the slipper.

f) Mechanical friction loss at the bearing:

$$p_{cb} = \frac{f_b F_b d_b}{2} \omega \tag{15}$$

where: F_b is the radial force acting on the bearing.

$$F_b = \frac{Z+1}{2} \cdot \frac{\pi}{4} \cdot d_z^2 p_d \tan\gamma \tag{16}$$

where: Z is the number of pistons, d_z is the piston diameter, p_d is the high-pressure oil pressure of the piston pump.

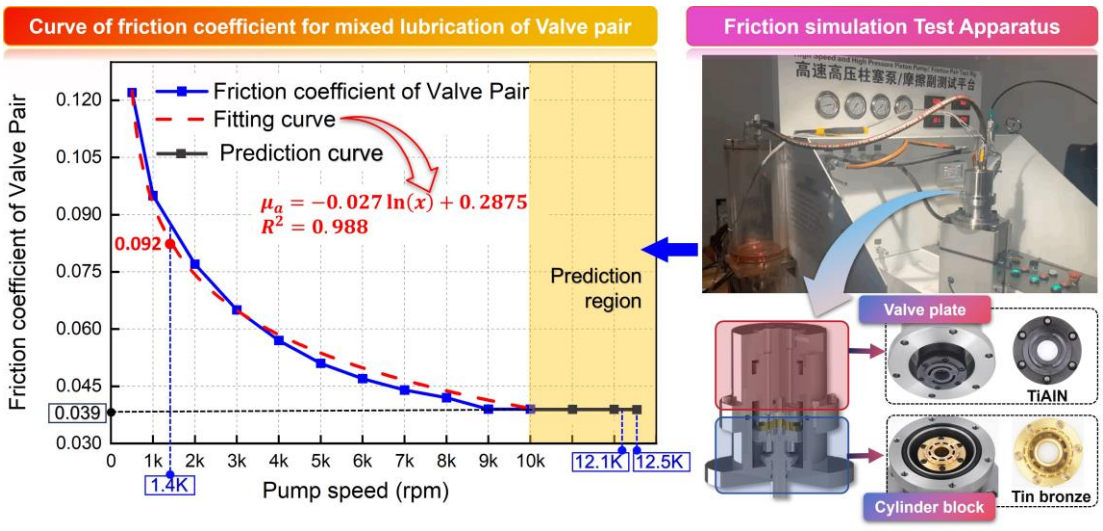

Figure 6 – Variation and fitting of the mixed friction coefficient of the valve plate pair of civil aircraft EHM with respect to speed

g) Friction loss at the valve plate pair

According to literature [22], the variation of the mixed friction coefficient at different speeds for the valve plate pair of this EHM is shown in the following graph. After fitting, it can be represented by the equation(16).

$$\mu_a = -0.027\ln(x) + 0.2875, \quad R^2 = 0.98 \tag{17}$$

In this case, the mechanical loss at the valve plate pair can be represented as:

$$p_{\mathrm{v}} = \mu_a \times N = \mu_a \times \frac{\pi\omega(2R_4R_3 - R_2R_1)R_c}{2}\Delta\mathrm{p} \tag{18}$$

where: μ_a is the mixed friction coefficient of the valve plate pair, N is the positive pressure at the valve plate pair, Δp is the pressure difference between the inlet and outlet oil, and R_c is the radius of the distribution circle of the kidney-shaped holes.

h) Oil stirring losses in the cylinder block of the axial piston pump and in the motor stator

$$P_{\mathrm{c\mu l}} = \frac{2\pi\mu\omega^2 l_r {R_r}^3}{t} \tag{19}$$

$$P_{\mathrm{c\mu t}} = 2\pi\lambda\rho {R_r}^2\omega^3 l_r \tag{20}$$

where μ is the fluid viscosity, l_r is the length of the rotating part, ω is the angular velocity, t is the radial length between the rotating part and the housing, λ is a coefficient related to the structure. In laminar flow conditions, the source of stirring losses is primarily due to liquid viscosity, which is greatly influenced by the fluid viscosity. However, in turbulent flow conditions, the cause of viscous friction is the fluid inertia.

The main structural parameters of the EHM are shown in Table 4 and Figure 5 (a):

Table 4 Main structura parameters of the EHM

Parameters		Symbol	Unit	Values
Kinematic viscosity		μ	Kg /ms	0.015
Outlet pressure		P_d	MPa	1, 11.78, 35
Inlet pressure		P_l	MPa	1
Number of piston		Z		9
swash plate inclination		β	°	9
Piston diameter		d_z	mm	7.5
Piston index circle radius		R_p	mm	14.65
Piston pump friction pair oil film height	Piston pair	δ_p	μm	10
	Slipper pair	δ_s	μm	10
	Valve pair	δ_v	μm	15
Coulomb friction factor under static pressure support	Ball hinge of piston pair	f_{ch}		0.005
	Slipper pair	f_{cs}		0.008
	Bearing	f_{cb}		0.005
Mixing friction factor of the valve pair		μ_a		Determined by the mixed friction state

By combining the above equations, the mechanical loss values under various operating conditions can be obtained, as shown in Table 5:

Table 5 Loss value under each operating condition W

Loss type		operating condition I @12500rpm 3.72NM	operating condition Ⅱ @12100rpm 0.98NM	operating condition Ⅲ @1400rpm 11.26NM
Volumetric Loss		265	can be ignored	1147.5
Valve plate loss		1531	137.53	1274
Frictional loss	Slipper	206.3	18.52	72.89
	Piston	45.19	16.39	0.03
	Piston ball hinge	34.46	3.09	12.17
	Bearing	12.34	2.2	8.8
Viscosity loss	Slipper	114.2	107.06	1.43
	Piston	0.66	0.62	0.01
stirring loss	PMSM	149.6	140.21	1.87
	Cylinder	3.42	3.21	0.04

3) Electromagnetic Loss

The electromagnetic loss generated during the operation of the motor dissipates in the form of heat energy, becoming a heat source during the main operation of the motor. It mainly includes iron loss, copper loss, and eddy current loss. Accurate analysis of the electromagnetic field is a prerequisite for accurately calculating temperature rise. When the temperature rises, the electromagnetic properties of certain materials may change, resulting in changes in the electromagnetic parameters of the motor. The influence of temperature on residual magnetism (B_r) and coercive force (H_C) is shown in (6) and (7). The copper loss of the winding under temperature variation can be expressed as:

$$B_r(t) = [1 + (T_{PM} - T_0)\alpha_{B\mathbf{r}}/100](1 - IL/100)B_{r0} \tag{21}$$

$$H_C(t) = [1 + (T_{PM} - T_0)\alpha_{Cj}/100](1 - IL/100)H_{c0} \tag{22}$$

$$P_{cu} = \sum_{i=1}^{3} I_i^2 R_a[1 + \alpha(T - T_0)] \tag{23}$$

Where B_{r0} and H_{C0} are the residual magnetism and coercive force at ambient temperature; $\alpha_{B\mathbf{r}}$ and α_{Cj} are the reversible temperature coefficients of B_r and H_C; IL is the irreversible loss rate of B_r; T_{PM} is the operating temperature of the magnet; T_0 is the initial winding temperature; R_a is the initial resistance; α is the resistance temperature coefficient; I_i is the effective value of phase current; T is the actual temperature during motor operation.

From the above equation, it can be seen that the winding resistance of the motor increases linearly with temperature, while the control current of the motor does not significantly increase with temperature. Therefore, the copper loss of the motor increases linearly with temperature. In addition, temperature has a significant impact on the permanent magnet, leading to irreversible demagnetization.

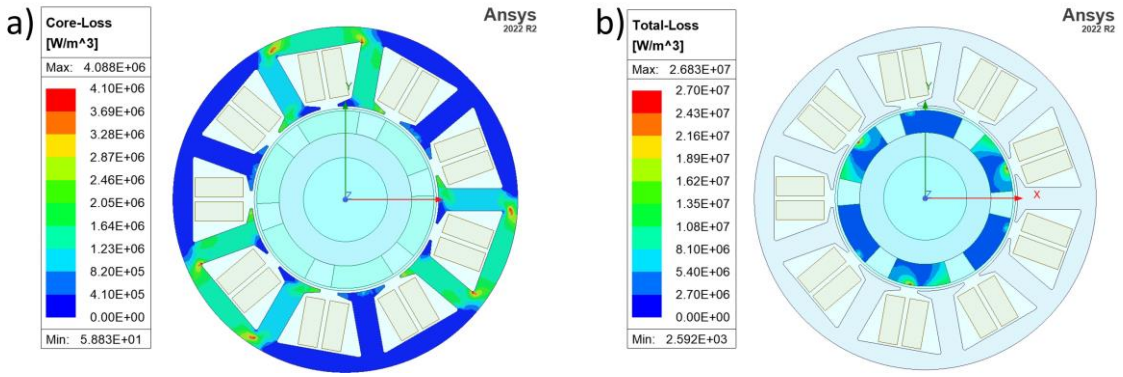

Figure 7 – Distribution of electromagnetic loss density

The electromagnetic losses are obtained through finite element analysis, and the density distribution of the stator and permanent magnet is shown in Figure 5 using electromagnetic analysis methods. It can be observed that the motor losses are unevenly distributed during actual operation. It can be seen that the stator loss density is not uniformly distributed: the tooth region has a higher loss density, the middle part of the yoke has a lower loss density, and due to the limitation of the outer diameter of the stator, the loss density is also higher in the outer periphery of the stator yoke, as shown in Figure 7 a); the external loss density of the permanent magnet is significantly higher than the internal loss density, as shown in Figure 7 b). However, traditional temperature rise analysis methods assume uniform distribution of losses in volume, which obviously cannot directly reflect the actual temperature distribution. Moreover, considering the influence of temperature on material electromagnetic properties, the losses in the windings and stator sections need to be calculated and assigned to the simulation model through a bidirectional coupling method. The specific method will be introduced in the next section.

2.3 Bidirectional analysis methods

In the coupling analysis process, the initial temperatures of various components of the motor in the initial state need to be determined first. Then, based on the magnetic field distribution and prototype

parameters, the losses of each component of the motor are calculated. The flow conditions of the motor in the flow field are analyzed, and the convective conditions and cooling boundaries of the temperature field are obtained. The non-uniform losses are mapped as heat sources into the temperature field solving domain, using the boundary conditions obtained from the input flow field. The solver simulates the motor temperature rise process in this time step, thereby determining the overall distribution of the motor temperature in the next moment. Based on the new temperature distribution of the motor, considering the changes in the parameters of the motor materials and fluid state under temperature influence, the distribution of the electromagnetic field and flow field of the motor is recalculated, and the cycle from the electromagnetic field and flow field to the temperature field is repeated. The calculations continue until the predetermined solution time is reached or the error between the initial preset temperature and the final coupled iterative temperature is less than 1%. Finally, the temperature rise curve of the motor during operation and the distribution of temperature field at each iteration are obtained. The specific coupling process is shown in Figure 8.

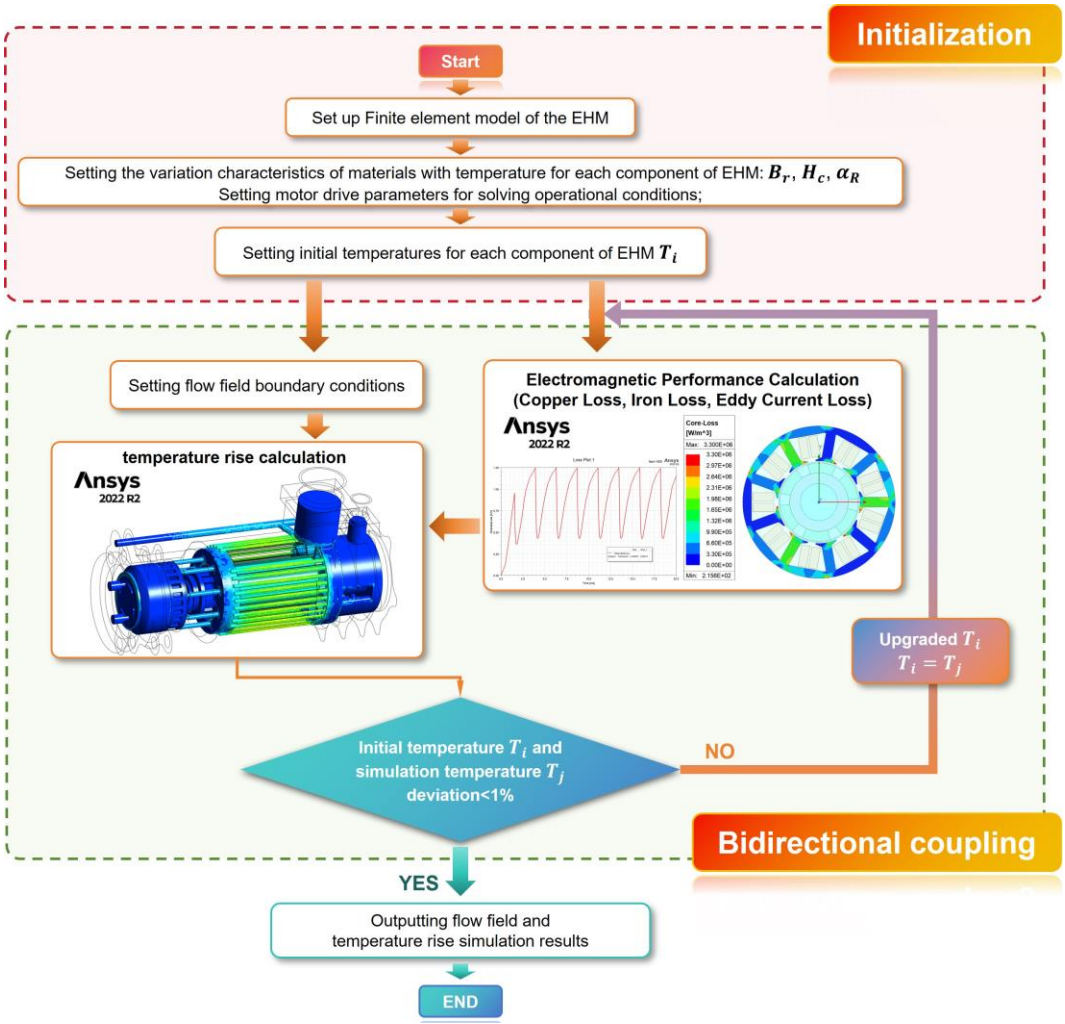

Figure 8 – Coupling Analysis process

2.4 Finite Element Simulation Preprocessing

2.4.1 Model Simplification

To accelerate simulation convergence while ensuring solution accuracy, the following simplifications were made to the EHM model:

(1) Internal components of the EHM, such as the cylinder body, shoe, piston, and tightening plug, have a minimal impact on oil suction and heat dissipation and were neglected.

(2) Chamfers, fillets, and other features that have little effect on simulation results but affect grid partitioning were removed from the components.

(3) The piston pump has a complex structure, and a simplified approach was applied by merging

stationary components.

(4) The bearing section was simplified based on the principle of equal equivalent flow area.

(5) The winding part was simplified by considering the insulation layer wrapped around the copper wire, taking into account the slot fill factor, and making adjustments to the thermal parameters of the insulation layer.

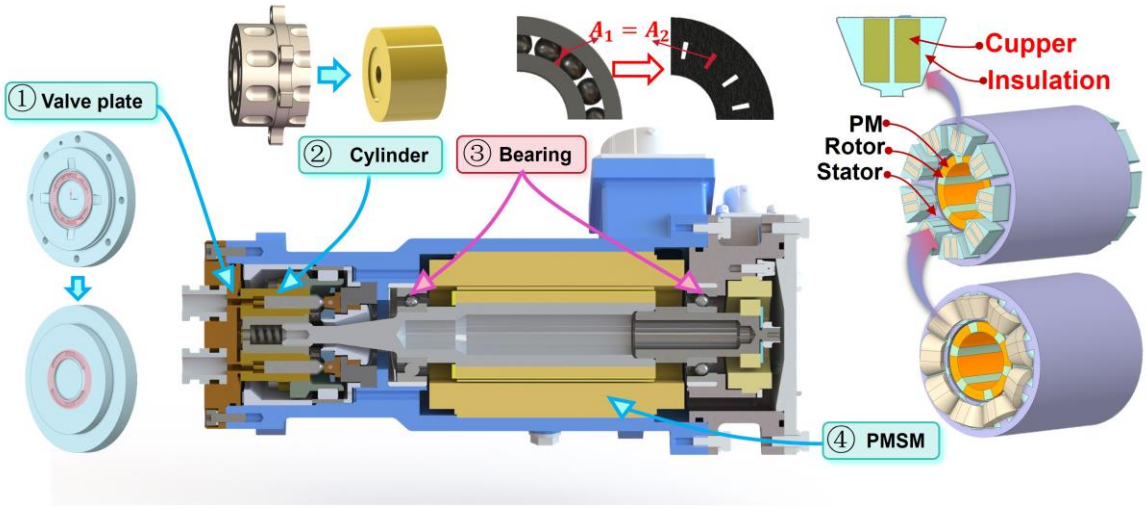

Figure 9 – EHM Model Simplification

2.4.2 Mesh Generation

The mesh generation was performed using ANSYS-Meshing. The overall mesh size was defined as 3mm, while different partitioning methods were applied for local regions with local refinement, such as the flow channel, motor winding, and insulation. The distribution component utilized a multi-scale model, and the overall mesh size was defined as 0.15mm. Due to the simulation of rotor oil churning effect using a sliding wall model, no dynamic mesh was set. The mesh partitioning of the fluid and solid domains is illustrated in Figure 10.

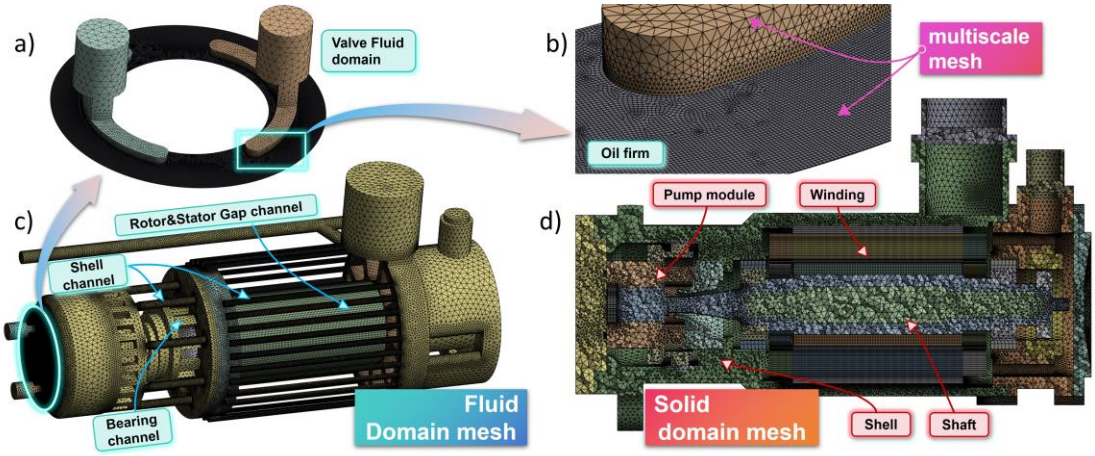

Figure 10 – EHM Mesh Generation

2.4.3 Finite Element Solution Settings

The relevant properties of the materials involved in the finite element simulation are shown in Table 6. The parameters of the insulation material were obtained through experimental data correction.

Table 6 Material Properties of EHM

Material name	component name	Density (kg/)	Thermal conductivity (W/(m℃))	Specific heat （J/(kg℃)）
Air	Outer air domain	1.29	0.023	1010
Skydrol Id-4	Hydraulic oil	1008	0.115	1880

7075 aluminum alloy	Shell	2810	150	960
2A12 duralumin	Barrier	2800	175	900
40CrNiMoA	Mian shaft	7830	22.2	480
DW310-35	Stator core	8500	20	480
Cu	Coil	8960	387.6	381
Smco26H	Mag	8400	12	130
1Cr17Ni2	Bearing	7750	22.6	460
S30408	Sheath of rotor	7930	16.3	500
carbon steel	Pump	8030	16.27	502.48
Polyimide	Equivalent winding insulation material	1400	381	2.8

Due to the motor being a wet motor, the internal cooling is achieved through forced convection, while the motor casing relies on natural convection for external cooling. Since the shaft, rotor, magnetic steel, and rotor sleeve rotate together as a single unit, the oil churning effect in the large coaxial flow field cannot be ignored. To simulate this phenomenon, a rotating wall boundary condition is employed in the simulation. The K-epsilon turbulence model and the Coupled solution method are selected. The inlet and outlet conditions, rotational speed of the rotating wall, and convective heat transfer coefficient of the EHM casing are set as shown in the table7.

The EHM casing comes into contact with the surrounding air, and heat is primarily dissipated to the ambient environment through natural convection on the surface of the housing and end cover. The influence of thermal radiation is neglected, and the convective heat transfer coefficient on the outer surface of the EHM casing is :

$$\alpha = 14(1 + 0.5\sqrt{v})^3 \sqrt[3]{\frac{t}{25}} \tag{24}$$

Where, v represents the air velocity that blows over the surface of the housing, and the ambient temperature is denoted as t. If simulating the onboard EHA (Electro-Hydrostatic Actuator) environment, the reference air velocity would be the airflow inside the aircraft wing's control surface compartment, which is typically less than 4.2m/s. If comparing with experimental data, the reference air velocity would be based on the laboratory wind speed. The variable t represents the ambient temperature.

Table 7 Simulation boundary conditions of flow field under different operating conditions

boundary conditions	Unit	operating condition I @12500rpm 3.72NM	operating condition II @12100rpm 0.98NM	operating condition III @1400rpm 11.26NM
Ambient temperature	℃	25	25	25
Rotor speed	rpm	12500	12100	1400
Coefficient of convective heat transfer of shell	W/(m²·K)	4	4	4
Inlet velocity	m/s	7.195	7.433	0.825
Inlet pressure	MPa	1	1	1
Inlet oil temperature	℃	35	35	35
outlet 1 mass flow	Kg/s	0.355	0.355	0.00756
outlet 2 mass flow	Kg/s	0.024	0.00185	0.03402

2.4.4 Bidirectional Coupling Settings

The thermal-magnetic bidirectional coupling is implemented based on the ANSYS Workbench platform. Maxwell calculates the electromagnetic losses in the motor based on the material properties and operating conditions. These losses are then mapped as heat sources into Fluent. Fluent, in conjunction with fluid boundary conditions and heat sources, calculates the temperature rise. The results from both Maxwell and Fluent are iteratively exchanged through the Feedback Iterator. The temperature rise results obtained from Fluent are fed back to Maxwell, where the electromagnetic properties of the materials are modified, and the heat source values are updated. The updated data is then imported back into Fluent for temperature rise calculations.

For a wet motor, its structure can be considered as an axial stretching of a certain face. Therefore, a 2D finite element method can be used to solve the losses of the wet motor, while a 3D finite element

method is employed to solve the overall temperature field of the EHM. The settings in Workbench are shown in the following figure.

Since the low-speed high-torque operating condition is the EHM's overloaded condition, there is a risk of excessive heat generation, which can impact the lifespan and output performance. Therefore, bidirectional coupling analysis is utilized to analyze the temperature rise of the entire EHM under this operating condition.

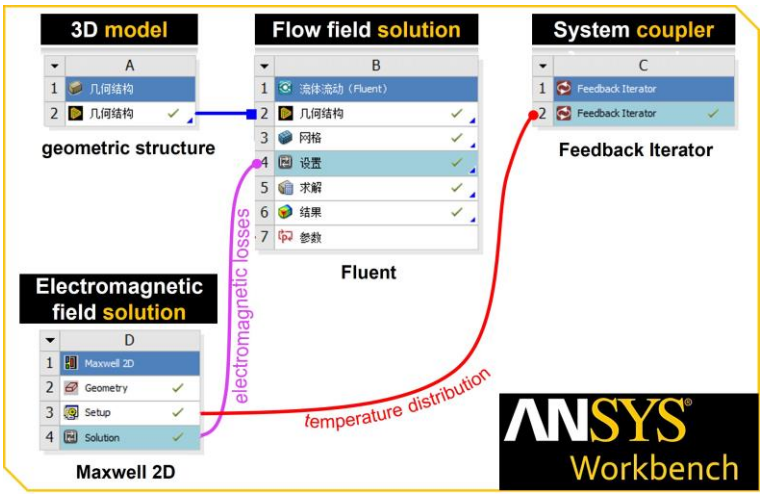

Figure 11 –ANSYS-Workbench Bidirectional Coupling Settings

3. Experimental Validation

3.1 Experimental Setup

In order to validate the accuracy of the simulation results, a temperature rise experimental platform was constructed. It mainly consists of an embedded temperature measurement system, data acquisition system, and load simulation system. The host computer obtains operating condition simulation instructions through a human-machine interface, controls the load simulation hydraulic system to perform load simulation, and simultaneously operates the EHM under specified operating conditions through a controller and driver. The embedded temperature measurement system collects temperature at characteristic points, and the data is transmitted to the host computer through the data acquisition system for data display and storage. Within the embedded temperature measurement system, a thermal resistance temperature sensor is embedded at the winding terminal and oil discharge port to measure the temperatures at two specific points, referred to as Point 1 and Point 2, respectively. The temperature of the EHM housing is measured using a thermal imaging camera, referred to as Point 3. The testing platform is shown in Figure 12.

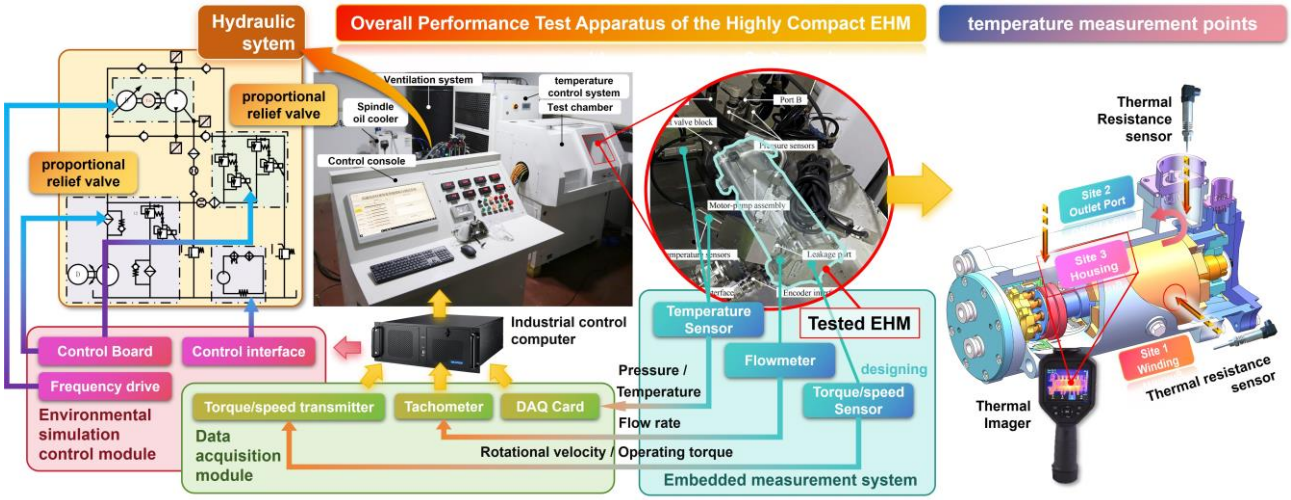

Figure 12 – The architecture of the test system

3.2 Comparison of Theoretical and Experimental Results

For the studied novel EHM, temperature measurements of characteristic points were obtained through performance testing at multiple operating points. Simultaneously, the temperatures of the corresponding characteristic points were calculated using the electromagnetic-thermal bidirectional coupled finite element model established in this study, as shown in Figure 13.

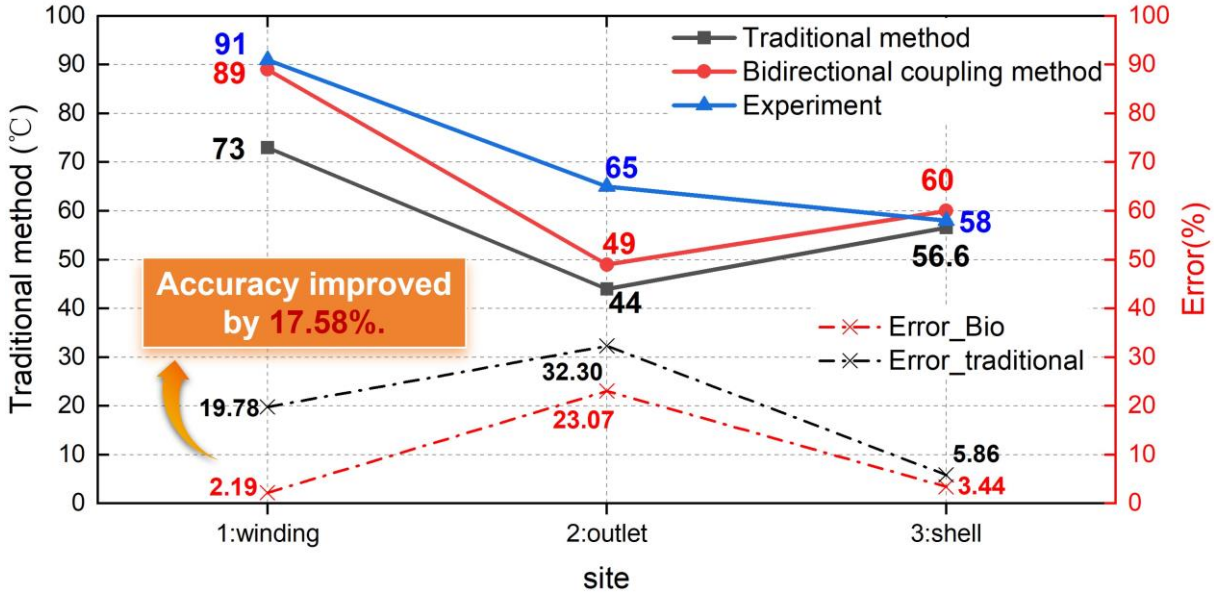

Figure 13 – The comparison between experimental data and bidirectional coupled simulation data under multiple operating conditions.

The EHM's temperature rise reaches a relatively stable state after running for 2 minutes under three typical operating conditions. The comparison between the simulation results and experimental results is shown in Figure 13.

Under the low-torque operating condition, the temperature rise mainly occurs at the winding location, with an experimental temperature of 91°C. The experimental temperatures at the housing and oil discharge port are 58°C and 65°C, respectively. Compared to the experimental results, the temperature error at the winding location using the bidirectional thermal-magnetic coupling method is 0.6°C. This error is within an acceptable range since the winding structure is derived from an equivalent winding, resulting in a discrepancy from the actual structure. The temperature errors at the oil discharge port and housing are 16°C and 2°C, respectively.

In contrast, using traditional temperature rise analysis methods, the temperature errors at the winding, housing, and oil discharge port are 18°C, 21°C, and approximately 3.4°C, respectively. The main cause of temperature errors in the traditional analysis is the significant error in calculating the motor copper losses due to the neglect of the variation in winding resistivity with temperature.

In summary, compared to the unidirectional coupling model, the bidirectional coupling model shows results that are closer to the measured values.

4. Analysis and discussion

4.1 Analysis of Electromagnetic-Thermal Bidirectional Coupling Results

Following the process depicted in Figure 9, electromagnetic-thermal flow coupling iterations were conducted to analyze the heat generation under the low-speed high-torque operating condition (i.e., speed of 1400 rpm and torque of 11.6 Nm). The iteration data is presented in Table 8, and the temperature difference between the final coupled iteration temperature and the initial preset temperature is less than 1%. At this point, the overall temperature of motor components remained below 90°C, with the highest temperature in the winding section reaching 89.02°C and an average temperature of 86.15°C. The maximum temperature for the permanent magnet was 36°C, while the stator reached a maximum temperature of 68°C.

Table 8 Coupling Iteration result ℃

Volume mean temperature	Initial temperature	Coupling result
Winding	20	86.15
Setting error	1%	

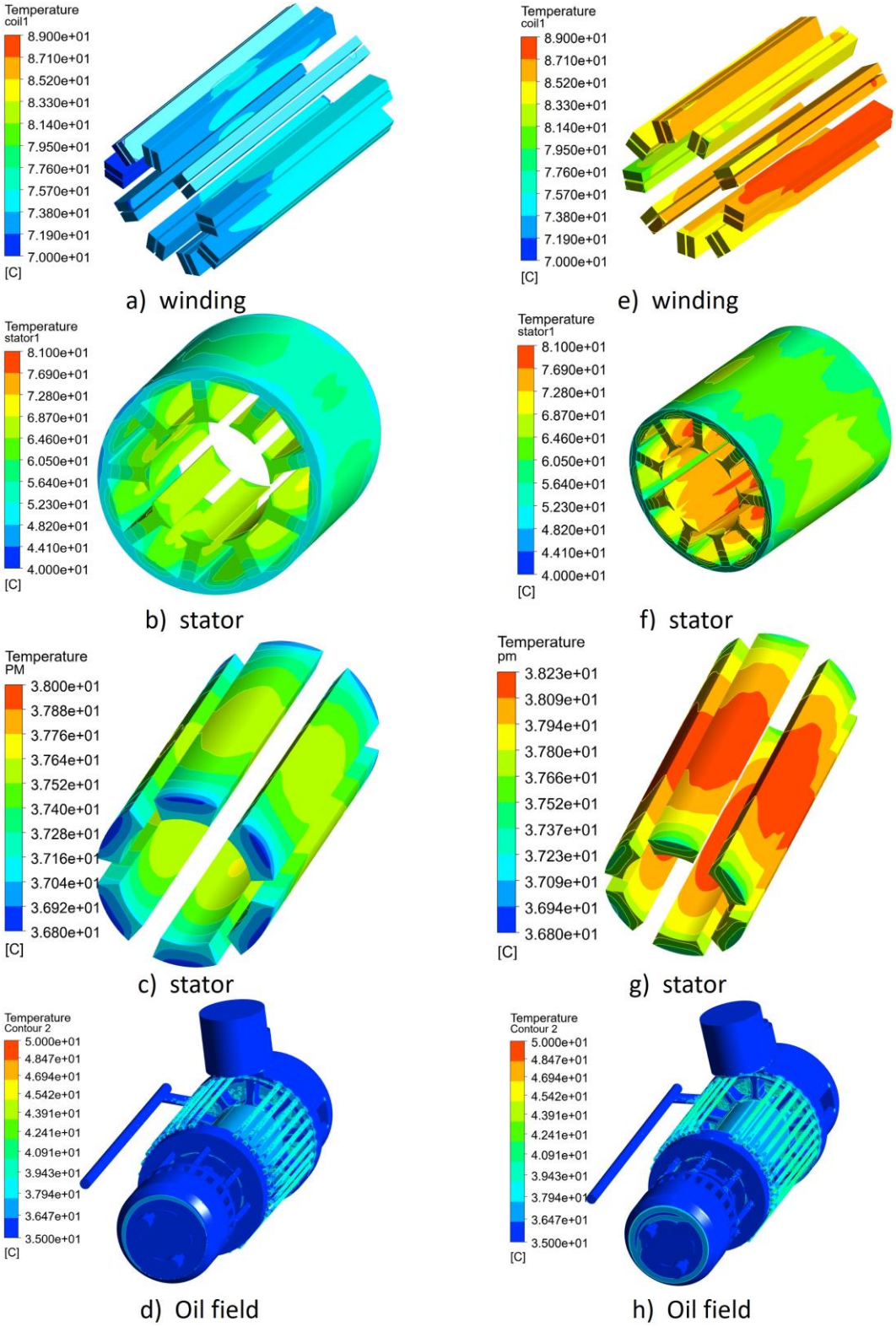

Figure 14 – The temperature contour plots of the traditional temperature rise method and the thermal-magnetic bidirectional coupling method are shown in the figure.

The temperature simulation results of the EHM under the low-speed high-torque operating condition are shown in Figure 14. By comparing the results of the magnetic-thermal coupled simulation method

(Figure 14 e), f) , g) , h)) with the traditional temperature field analysis method (Figure 14 a), b), c), d)), it can be observed that the overall temperature of the major components of the EHM is relatively high. However, the expected temperature difference between the tooth section and the yoke section, caused by the higher loss density in the tooth section of the stator, is not evident in the stator temperature contour plot. This is because under the low-speed high-torque operating condition, the heat generation at the winding is much greater than that at the stator. As a result, the stator temperature field is dominated by the heat generated at the winding, and the temperature differences caused by uneven stator losses are not reflected.

In conclusion, the temperature rise analysis using the electromagnetic-thermal bidirectional coupling method provides a closer approximation to the actual operating conditions of the motor.

4.2 Temperature Rise Analysis under Different operation Conditions

Although the traditional temperature rise algorithm may not have high accuracy, it can still reflect the temperature variation trends of the same components under different operating conditions and distinguish the location of the highest temperature from the temperature contour plots. The temperature distributions of the EHM under different operating conditions are shown in Figure 14.

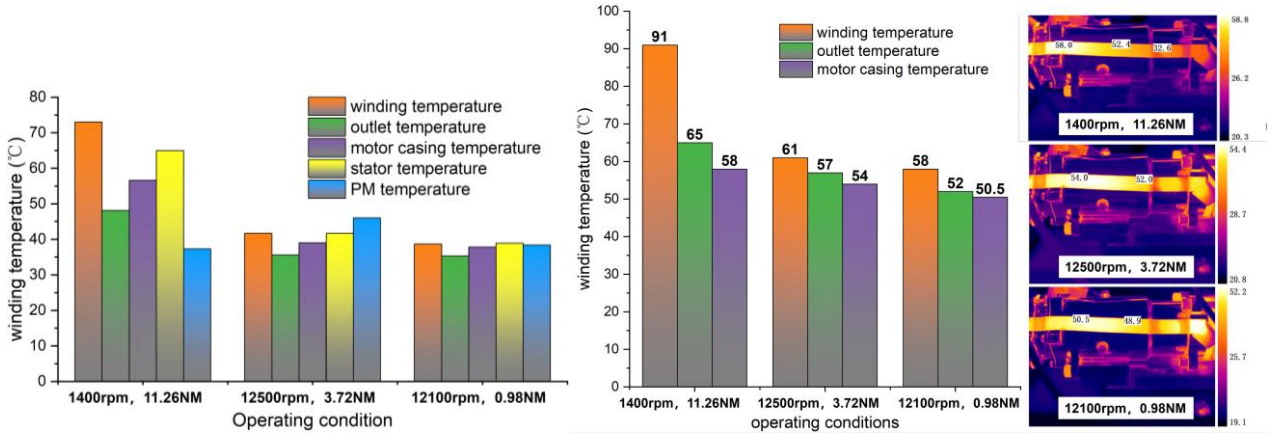

(a) Simulation results (traditional method) (b) Experimental results

Figure 14 – The temperature contour plots of the traditional temperature rise method and the thermal-magnetic bidirectional coupling method are shown in the figure.

From the above figure, it can be observed that the temperature rise results obtained by the traditional temperature rise calculation method are higher for the housing compared to the oil temperature rise results. This is different from the experimental results. The reason for this discrepancy is that in actual situations, there is a very small gap between the stator and the housing due to manufacturing techniques and assembly errors. This gap is filled with cooling oil, which means that the heat exchange between the stator and the housing occurs through the oil. Therefore, the stator temperature is higher than the oil temperature, which is higher than the housing temperature. However, in the simulation, to ensure the accuracy of results in critical areas such as the winding, the consideration of computational resources takes precedence. Therefore, the simulation does not model this assembly gap, except for the flow channels, and assumes a direct contact heat exchange path between the stator and the housing. As a result, the simulated stator temperature is higher than the housing temperature, which is higher than the oil temperature.

The experimental and simulation results show that the highest temperature is consistently observed at the winding under all three typical operating conditions. Combining the simulation and experimental results, it can be concluded that under the low-speed high-torque operating condition, the copper loss and auxiliary loss in the commutation region of the EHM are significantly higher than other losses. Additionally, due to poor heat dissipation at the stator outlet, the temperature around the winding is the highest. Under the high-speed low-torque operating condition, the auxiliary losses in the commutation region of the EHM are significantly higher than other losses. However, due to the presence of the rotor sleeve, the heat dissipation around the permanent magnet is insufficient, resulting in relatively high temperatures in that region.

4.3 Analysis of Heat Generation Interactions among Motor-Pump Components

In previous studies on the temperature field of EHM, the complex structure of the piston pump and the oil stirring effect are often simplified, and sometimes the heat generation of the pump is not considered at all, focusing only on the temperature field of the wet motor section. To validate the rationality of the aforementioned simplifications, it is necessary to investigate the degree of mutual heat generation interactions between the motor and pump. If it can be proven that the mutual interactions between them are minimal, subsequent studies on thermal characteristics can independently calculate the pump and motor, greatly reducing the workload.

To explore the extent of the pump's heat generation impact on the temperature field of the motor section, the operating condition with the highest pump heat generation, namely the high-speed low-torque condition, was selected. The pump heat generation was set to zero, and the temperature variations of the motor winding, stator, and permanent magnet under this condition are shown in Figure 15(a)(b)(c). In comparison, the temperature distributions of the above three points under normal operating conditions are shown in Figure 15(d)(e)(f). The comparison of the maximum temperatures at the respective locations is presented in Table 9.

Table 9 Comparison with the temperature distribution under normal operating conditions℃

Site	operating condition I		Error %
	normal	Zero pump loss	
Winding	41.76	41.74	0.05
Stator	41.73	41.71	0.05
Sheath	45.45	45.38	0.15

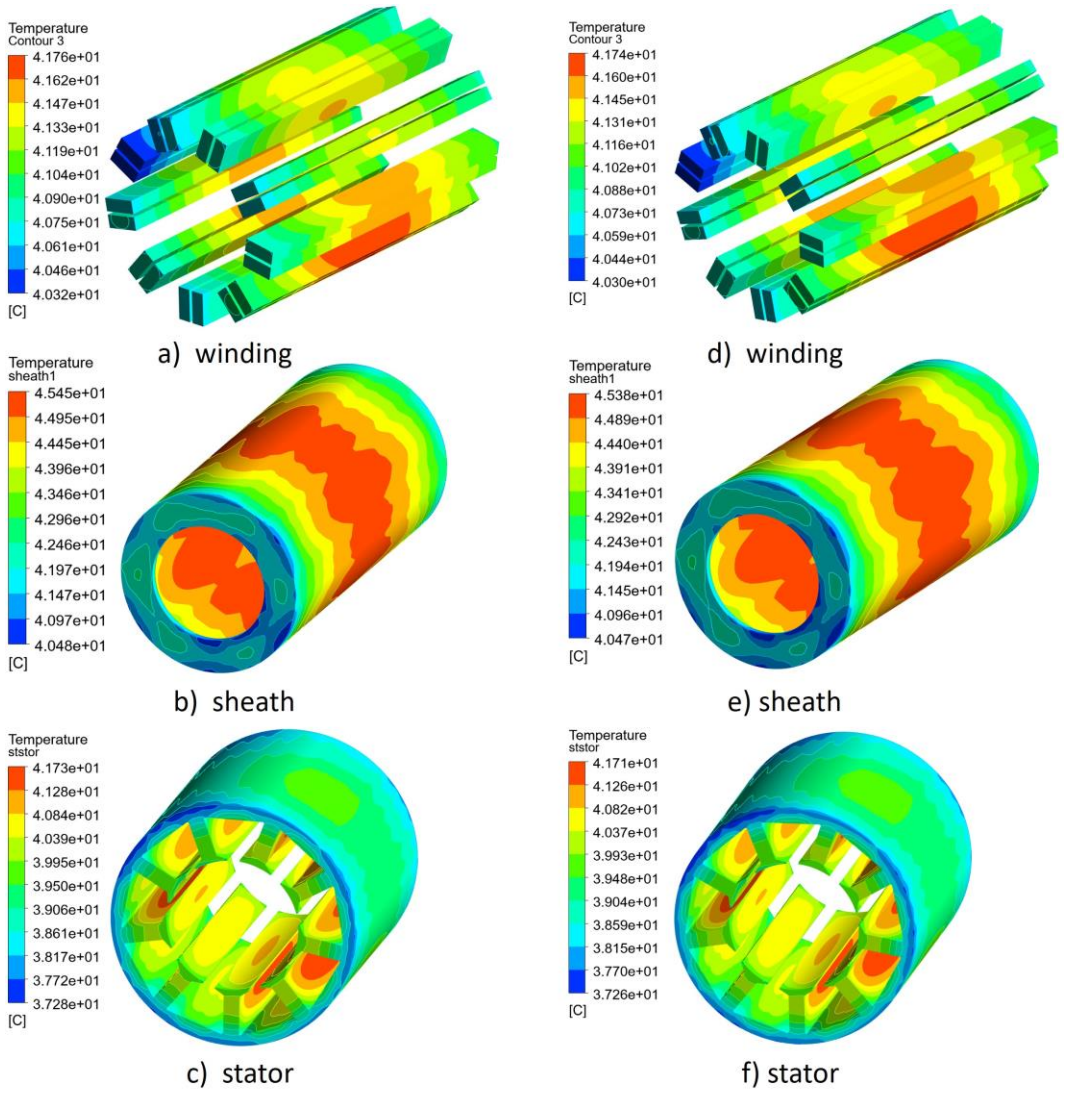

Figure 15 – The temperature contour plots of key locations in the motor

From the above table, it can be seen that when the pump heat generation is set to zero, the temperatures at key locations in the motor (winding, stator, and sleeve) are lower than under normal operating conditions. This confirms the validity of the results, indicating that the influence of pump heat generation on the temperature distribution of key motor locations is less than 1.5%. This demonstrates that the impact of the pump on the motor's temperature field is relatively small, justifying the simplifications made in previous studies. Further analysis reveals that the minor impact is primarily due to the fact that heat exchange between the pump and motor occurs through the oil, which has a relatively low specific heat capacity and thermal conductivity. Additionally, the lower internal leakage and resulting lower axial oil flow velocity contribute to the lower degree of heat coupling.

4.4 Efficiency Analysis of the Piston Pump Used in EHM

By incorporating the loss model, it is possible to calculate the volumetric efficiency, mechanical efficiency, and overall efficiency of the pump under "low speed high torque" and "high speed low torque" conditions. Comparing these calculated efficiencies with the total efficiency obtained from experimental measurements allows for the validation of the accuracy of the loss model, essentially verifying the correctness of the selected friction factor. Since the experimental data was obtained after improving the material pairing of the distribution components, the friction factor differs from the results shown in Figure 6. Therefore, the friction losses of the distribution components are calculated using Method 1 (Equation (2)), as detailed in reference [17]. The results are presented in Table 10. The comparison between the pump efficiency obtained from the loss model and the efficiency measured in experiments is shown in Figure 16, demonstrating a high level of agreement between the two, It can be seen that the coincidence of the two is high, indicating that the Coulomb friction factor is close to the real value. Secondly, it can be seen from the results that the efficiency simulation results under high speed and low torque conditions are smaller than the experimental results, and the efficiency simulation results under low speed and high torque conditions are larger than the experimental results. This is because the lubrication condition under high speed conditions is better and the Coulomb friction factor is lower, while the lubrication condition under low speed and high torque conditions is worse and the Coulomb friction factor is higher. In the simulation, the friction factor is the same under both conditions. Hence the result.

Table 10 Calculation of Reactive Power Losses for Valve pair based on Equation (2)

Work condition		Operation condition I @12500rpm 3.72NM	Operation condition III @1400rpm 11.26NM
power losses in valve pair	Coulomb friction loss/W	196.35	69.36
	Viscous losses/W	587.66	7.37
The Coulomb friction coefficient under hydrostatic lubrication		0.05	0.05

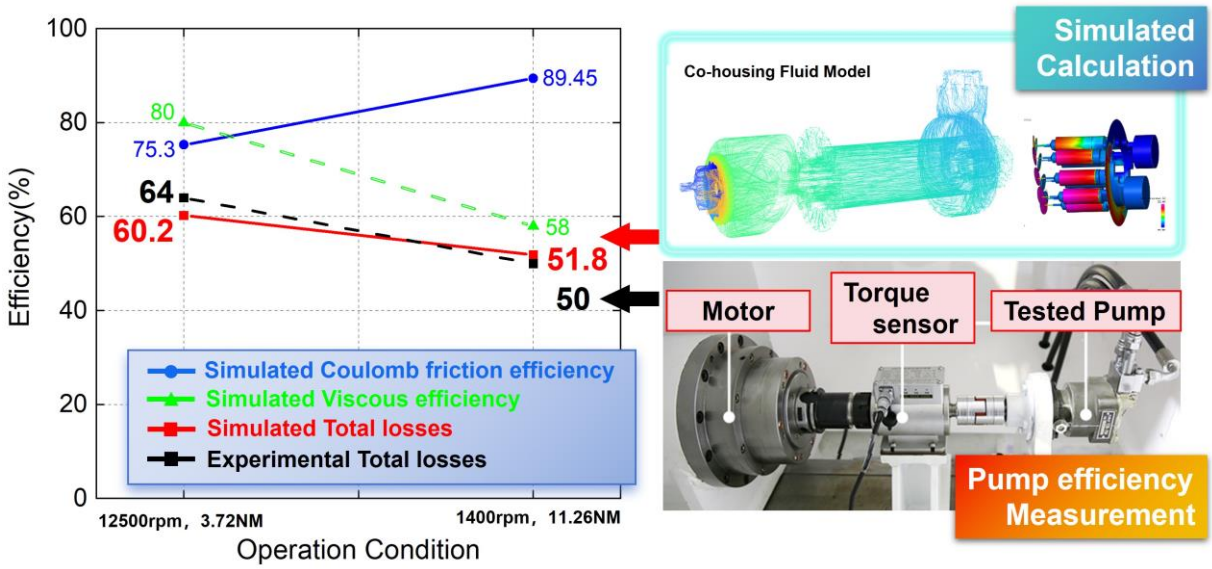

Figure 16 – Comparison of pump efficiency between simulation and experiments

5. Conclusion and prospective

The main contributions of this paper can be summarized as follows: "Assessment of losses under variable operating conditions" and "Electromagnetic-Thermal Bidirectional Coupling Method." Firstly, based on previous experiments, a new evaluation method for friction losses in the commutation region of the EHM under variable operating conditions is proposed. Additionally, a magnetic-thermal bidirectional coupling method is introduced, which considers the influence of temperature on the electromagnetic characteristics of the magnets and the uneven distribution of losses in various components during actual motor operation. The developed multi-field electromagnetic-thermal bidirectional coupling model achieves a 17.58% improvement in accuracy compared to traditional temperature rise calculation methods. This provides a feasible approach for establishing high-precision temperature field simulation models. The main conclusions of this paper are as follows:

(1) Under the coaxial large flow field, the mutual heat generation interaction between the pump and motor is relatively low. Subsequent studies can independently analyze the temperature fields of the pump and motor using finite element analysis, which significantly reduces the workload while ensuring a certain level of accuracy.

(2) The accuracy analysis method of bidirectional coupling improves accuracy and better simulates the influence of uneven loss density on heat generation.

(3) Under the low-speed high-torque operating condition, the highest temperatures are observed at the winding and stator, while under the high-speed low-torque operating condition, the temperature is higher at the permanent magnet.

Further research can be conducted in the following areas:

(1) Optimize the thermal structures of the EHM's permanent magnets and stator based on temperature rise data obtained from multiple operating conditions.

(2) Although this study includes a fitted analysis of mixed friction losses in the commutation region based on experimental data, the temperature rise in that region has not been experimentally verified. Furthermore, additional experimental research should be conducted to understand the mixed friction state in the hydraulic pump, focusing on the piston pair and shoe pair.

(3) The simplification of the winding in this study can be further refined in future research to make the simulation model more closely resemble the actual conditions.

6. Contact Author Email Address

Mail to: 19182716@buaa.edu.cn

7. Copyright Statement

8. References

[1] Zhao J, Fu J, Li Y, et al. Flow characteristics of integrated motor-pump assembly with phosphate ester medium for aerospace electro-hydrostatic actuators[J]. *Chinese Journal of Aeronautics*, 2022.

[2] Zhao S, He J, Zhang Y. The study on the dynamic capability of an electro-hydrostatic actuator to drive a large inertia load[A]. *2016 IEEE International Conference on Aircraft Utility Systems (AUS)*[C].836–841, 2016.

[3] Bruzzese C, Tessarolo A, Mazzuca T, et al. A closer look to conventional hydraulic ship actuator systems and the convenience of shifting to (possibly) all-electric drives[A]. *2013 IEEE Electric Ship Technologies Symposium (ESTS)*[C]. Arlington, VA: IEEE, 220–227, 2013.

[4] Liao J, He L, Chen Z, et al. Overview of submarine steering system noise[J]. *Chinese Journal of Ship Research*, 17(5): 74–84, 2022.

[5] Karanović V, Jocanović M, Jovanović V. Review of Development Stages in the Conceptual Design of an Electro Hydrostatic Actuator for Robotics[J]. *Acta Polytechnica Hungarica* , 11(5) , 2014.

[6] Raghavendra D R. Applications of EH Servo Systems[A].D.R. Raghavendra. *Electrohydraulic Servo Systems: Applications, Design and Control*[M]. Singapore: Springer Nature, 43–90, 2023.

[7] Sun D, Dong C, Li Hongyan, et al. Performance study of a high-speed small-displacement servo motor pump[J]. *Manned Spaceflight*, 29 (2) : 251-257, 2023.

[8] Liu L, Zhang P, Zhao S, et al. A test method for the static and dynamic characteristics of Servo-Motor-Pumps[A].2018(CP743) ,2018.

[9] Jin W, Guo H, Xu J. Design of high-speed wet-type permanent magnet synchronous motor considering oil frictional loss[A]. *2020 IEEE Energy Conversion Congress and Exposition (ECCE)*[C]. 1371–1378, 2020.

[10] Crowder R, Maxwell C. Simulation of a prototype electrically powered integrated actuator for civil aircraft[J]. Proceedings of the Institution of Mechanical Engineers, Part G: *Journal of Aerospace Engineering*, 211(6): 381–394, 1997.

[11] Powell D J, Atallah K, Jewell G. Thermal Modeling of Flooded Rotor Electrical Machines for Electro-Hydrostatic Actuators[A]. *2007 IEEE International Electric Machines & Drives Conference*[C]. Antalya, Turkey: IEEE 1632–1637, 2007.

[12] Gao, Sun, Zhuang. Research on multi-field coupling self-cooling characteristics of hydraulic motor pump[J]. *Aeronautical Science and Technology*,34 (10): 100-106, 2023.

[13] Zhang Y. Integrated thermodynamic modeling and structural optimization of oil-immersed motor pump[D]. Yanshan University, 2022.

[14] Tang H, Yin Y, Ren Y, et al. Impact of the thermal effect on the load-carrying capacity of a slipper pair for an aviation axial-piston pump[J]. *Chinese journal of aeronautics*, Elsevier Ltd, 31(2): 395–409, 2018.

[15] Tameemi A. Windage Losses Calculation and Performance Estimation for Wet Airgap PM Machines[A]. *2022 IEEE International Power and Renewable Energy Conference (IPRECON)*[C]. Kollam, India: IEEE, 1–6, 2022.

[16] Wen X, Yue L. Design of a new electromechanical protection device [J].*Technological innovation and application* (13) : 77-78, 2017.

[17] Zhu D, Fu Y, Fu J, et al. Power losses and thermal analysis of a designed Electro-Hydraulic Pump[A]. *2017 IEEE International Conference on Mechatronics and Automation (ICMA)*[C]. 728–733,2017.

[18] Bai G, Zhao H. Study on the influence of cooling channel structure on the temperature rise of motor pump[J]. *Journal of Zhengzhou University (Engineering Edition)*, 42 (4): 53-57, 2021.

[19] Chen S, Zhang Q, He B, et al. Thermal Analysis of High Density Permanent Magnet Synchronous Motor Based on Multi Physical Domain Coupling Simulation[J]. *Journal of Electrical Engineering and Technology*, The Korean Institute of Electrical Engineers, 2017, 12(1): 91–99.

[20] Hu X, Shi G, Lai Y, et al. Temperature Rise Calculation of the High Speed Magnetic Suspension Motor Based on Bidirectional Electromagnetic–Thermal–Fluid Coupling Analysis[J]. *Machines*, 2023, 11(3): 364.

[21] Guo C, Long L, Wu Y, et al. Electromagnetic-thermal coupling analysis of a permanent-magnet in-wheel motor with cooling channels in the deepened stator slots[J]. *Case Studies in Thermal Engineering*, 2022, 35: 102158.

[22] Zhao J. Optimized Design and Experimental Research of High-Speed High-Pressure Axial Piston Pump for Aerospace EHA[D]. Beihang University, 2021.